

PreCM: The Padding-based Rotation Equivariant Convolution Mode for Semantic Segmentation

Xinyu Xu, Huazhen Liu, Huilin Xiong, *Member, IEEE*,
Wenxian Yu, *Senior Member, IEEE*, and Tao Zhang* , *Member, IEEE*

Abstract—Semantic segmentation is an important branch of image processing and computer vision. With the popularity of deep learning, various deep semantic segmentation networks have been proposed for pixel-level classification and segmentation tasks. However, the imaging angles are often arbitrary in real world, such as water body images in remote sensing, and capillary and polyp images in medical field, and we usually cannot obtain prior orientation information to guide these networks to extract more effective features. Additionally, learning the features of objects with multiple orientation information is also challenging, as most CNN-based semantic segmentation networks do not have rotation equivariance to resist the disturbance from orientation information. To address the same, in this paper, we first establish a universal convolution-group framework to more fully utilize the orientation information and make the networks rotation equivariant. Then, we mathematically construct the padding-based rotation equivariant convolution mode (PreCM), which can be used not only for multi-scale images and convolution kernels, but also as a replacement component to replace multiple convolutions, like dilated convolution, transposed convolution, variable stride convolution, *etc.* In order to verify the realization of rotation equivariance, a new evaluation metric named rotation difference (RD) is finally proposed. The experiments carried out on the datasets Satellite Images of Water Bodies, DRIVE and Floodnet show that the PreCM-based networks can achieve better segmentation performance than the original and data augmentation-based networks. In terms of the average RD value, the former is 0% and the latter two are respectively 7.0503% and 3.2606%.

Index Terms—PreCM, rotation equivariance, convolution mode, data augmentation, semantic segmentation.

I. INTRODUCTION

SEMANTIC segmentation has been a fundamental and challenging task in computer vision for many years [1]. Since it can provide category information at the pixel level, it has been widely used in various fields, such as autonomous vehicles [2], water detection [3], road segmentation [4], and defect detection [5].

Within the context of traditional machine learning, semantic segmentation methods are normally constructed as classifiers, like Support Vector Machine (SVM) [6] and Random Forest (RF) [7]. In addition, considering the use of texture information to ensure the consistency between pixel labels,

context models such as Markov Random Fields (MRF) [8] and Conditional Random Fields (CRF) [9] are also utilized as classical frameworks for semantic segmentation. Although these algorithms are convenient and easy to implement, their poor feature extraction ability limits their generalization capability and segmentation accuracy.

With the development of deep learning, CNNs have proven their ability to extract more advanced features of images for semantic segmentation. Specifically, the translation equivariance of convolution kernels enables CNNs to better capture spatial features in images [10]. In [11], Long *et al.* used CNN-based fully convolutional networks to produce correspondingly-sized output with efficient inference and learning for semantic segmentation. Chen *et al.* [12] combined deep convolutional networks, atrous convolution, and fully connected conditional random fields to achieve semantic segmentation. Yang *et al.* [13] proposed Densely connected Atrous Spatial Pyramid Pooling (DenseASPP) for street scenes segmentation, which connected a set of atrous convolutional layers in a dense way to produce multi-scale features. Although these networks have achieved significant success in different semantic segmentation tasks, the convolutions often fail to guarantee the rotation equivariance of networks. So, when extracting the pose and texture features of objects, the networks are inevitably affected by the orientational information [14]. To tackle this issue, some works have been done from two aspects, i.e., extending data and designing networks. For the former, data augmentation technology is frequently utilized. In [15], Mikołajczyk *et al.* investigated the influence of multiple data augmentation methods on the image classification task, and proposed a new data augmentation method. Choi *et al.* [16] presented a data augmentation method based on Generative Adversarial Networks (GANs), which could enhance the performance of segmentation networks on the target domain. Olsson *et al.* [17] developed a semi-supervised semantic segmentation algorithm that used ClassMix, a new data augmentation technique to generate augmentation by mixing unlabeled samples. Although data augmentation technology can effectively help networks reduce their attentions to irrelevant features by introducing various rotated data, it also has two obvious limitations. One is the more orientation changes are considered, the more time costs and calculation budgets need to be consumed [18]. The other is adding rotated samples during the training stage only can make the segmentation results approximate to rotation equivariance.

In regard to designing networks, existing works mainly focus on the study of the rotation equivariance of $\{0^\circ, 90^\circ,$

*Corresponding author

This paper was supported in part by XXX.

X. Xu, T. Zhang, H. Xiong, and W. Yu are with the Shanghai Key Laboratory of Intelligent Sensing and Recognition, School of Sensing Science and Engineering, Shanghai Jiao Tong University, Shanghai 200240, China.

H. Liu is with the Intelligent Photoelectric Sensing Institute, School of Sensing Science and Engineering, Shanghai Jiao Tong University, Shanghai 200240, China.

$180^\circ, 270^\circ$ [19]–[22]. This is because, when performing rotation operations, images typically require resampling with the interpolation technique, like Bilinear Interpolation. Therefore, the rotation equivariance of the angles except for $\{0^\circ, 90^\circ, 180^\circ, 270^\circ\}$ is hard to accomplish [23]. Even so, for these works, strict constraints on the sizes of images and convolution kernels as well as the hyperparameters (e.g., stride and padding) are still needed [19], which in turn limits their further applications. Hence, it is necessary and meaningful for us to continue exploring how to keep the rotation equivariance of networks without these limitations. For this goal, this paper proposes one padding-based rotation equivariant convolution mode (PreCM), which thoroughly solves the rotation equivariance issue of $\{0^\circ, 90^\circ, 180^\circ, 270^\circ\}$ from the viewpoint of mathematics. Owing to the strict mathematical derivations, PreCM can be directly used as a replacement component to replace traditional convolutions, such as dilated convolution, transposed convolution, variable stride convolution, and so on.

In a nutshell, our contributions are three-fold:

- Based on the group theory, we first build a rotation equivariant convolution-group framework to extract the features related to orientational information, and also mathematically prove its rotation equivariance.
- For the proposed rotation equivariant convolution-group framework, we further give a concrete implementation, i.e., designing the padding-based rotation equivariant convolution mode (PreCM) that can not only be used as a replacement component to replace convolution operations for making networks rotation equivariant, but also realize the rotation equivariance under feature maps and convolution kernels of different scales as well as networks of different hyperparameters.
- To verify the effectiveness of PreCM, a new quantitative metric named RD (rotation difference) is correspondingly proposed. The experimental results carried out on three different segmentation tasks, i.e. binary, small-sample, and multi-class segmentations, prove the effectiveness of PreCM in semantic segmentation. Also, in comparison with the data augmentation-based networks, the PreCM-based networks show better segmentation performance without increasing the training samples.

The rest of this paper is organized as follows. Related work is discussed in Section II. Section III describes the methodology. The experimental results and analyses are given in Section IV. Section V concludes this paper.

II. RELATED WORK

In this section, the works related to semantic segmentation networks and rotation equivariance are introduced.

A. Semantic Segmentation Networks

As said before, CNNs have become one key tool for us to realize semantic segmentation. The CNN-based methods can provide pixel-level segmentation of images, enabling the advanced semantic understanding of images [24]. In this vein, Ronneberger *et al.* [25] proposed the network U-net for biomedical image segmentation. Badrinarayanan *et al.* [26].

presented a novel and practical deep fully convolutional neural network SegNet for semantic pixel-wise segmentation. Zhao *et al.* [27] designed the pyramid scene parsing network PSPNet with the global context information. Chen *et al.* [28] built the network DeepLab that used dilated convolution and fully connected CRFs to achieve semantic segmentation.

In addition, to reduce the consumption of time, many lightweight semantic segmentation networks with few parameters are also constructed. For example, Paszke *et al.* [29] built an efficient deep neural network architecture named Enet, which was specifically created for the tasks requiring low latency operation. In [30], Romera *et al.* proposed a deep architecture Erfnet that can run in real time while providing accurate semantic segmentation. Yu *et al.* [31] designed an efficient and effective network BiSeNet V2 with a good trade-off between speed and accuracy, wherein the spatial details and categorical semantics were separately treated so as to achieve real-time semantic segmentation. Wang *et al.* [32] presented a lightweight network LEDNet to deal with the problem of extensive computational burden for the task of real-time semantic segmentation.

In a summary, semantic segmentation is an important branch of scene interpretation. How to establish more efficient semantic segmentation networks is still worthy studying.

B. Rotation Equivariant Networks

In the real world, some images, e.g., remote sensing images, are usually obtained from arbitrary angles, which makes their semantic information extraction potentially sensitive to orientation. Therefore, some researchers study the rotation equivariance of networks for enhancing the feature extraction ability. In [33], Marcos *et al.* proposed the rotation equivariant vector field network (RotEqNet), which implemented classification, segmentation, orientation estimation and matching tasks by applying each filter at different orientations. Deng *et al.* [34] introduced a general framework built on the top of vector neuron representations to create SO(3)-equivariant neural networks for pointcloud processing.

Recently, with the help of group theory, Cohen *et al.* [19] proposed group equivariant convolutional neural networks G-CNNs, where the group equivariant convolution of the angles $\{0^\circ, 90^\circ, 180^\circ, 270^\circ\}$ was the core and put forward for the first time. Since then, G-CNNs have been widely used and improved. For instance, in [20], Li *et al.* further developed a deep rotation equivariant network consisting of cycle layers, isotonic layers, and decycle layers, which applied rotation transformation to filters rather than feature maps. Han *et al.* [35] designed a rotation-equivariant detector ReDet, wherein G-CNNs were introduced as well. Weiler *et al.* [36] built steerable filter CNNs (SFCNNs), which adopted the group convolutions to guarantee an equivariant mapping. Although this group equivariant convolution is extensively used, the networks derived from it require strict restrictions on the size of images and convolution kernels. From the perspective of networks' input and output, these restrictions indicate that we have to resample the images, leading to a loss of context information. From the perspective of network utilization, they

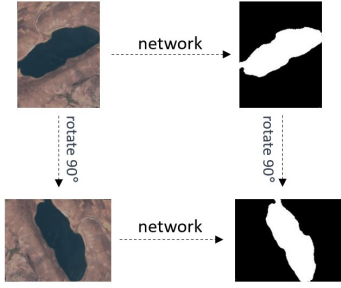


Fig. 1. An example of a network that has rotation equivariance.

make many classical combinations of feature map sizes and convolution kernel parameters (such as 256×256 images, 3×3 convolution kernel with dilation=1, stride=2, padding=1) as well as some classical convolutions (like variable stride convolution) hard to work. Therefore, it is necessary for us to redesign a new group equivariant convolution associated with $\{0^\circ, 90^\circ, 180^\circ, 270^\circ\}$.

III. METHODOLOGY

A. Rotation Equivariance

For various CV tasks, the concept of rotation equivariance is the same, that is, when rotating the images, the extracted features are also simultaneously rotated. More detailedly, after rotating an image, its features will do the same ordered rotation transformation. Fig. 1 gives an example of a network that has rotation equivariance. Mathematically, the rotation equivariance can be defined as [19]

$$g(\sigma x) = \sigma g(x), \quad (1)$$

where σ is a transformation operation, $g(\cdot)$ represents a function that maps one feature space to the other feature space, and x represents the input image.

From Eq. (1), one can find that the image rotation and mapping are commutative, that is, if the feature map obtained by rotating the image first and then mapping it is the same as the feature map obtained by mapping the image first and then rotating it. If Eq. (1) is satisfied, then the network has rotation equivariance.

B. Rotation Equivariant Convolution-group Framework

The group theory proposed in [19] has already shown great potential to keep the networks rotation equivariant. Inspired by it, we here construct a rotation equivariant convolution-group framework, which mainly contains three layers. Noted that, different from the previous applications of group theory on networks, we use group theory to represent the processing modes of features and information, rather than feature maps.

First of all, a four-element cyclic group $\sigma = \{\sigma_0, \sigma_1, \sigma_2, \sigma_3\}$ is introduced, satisfying

$$\sigma_i^{-1} = \sigma_{(4-i) \bmod 4}, \quad (2)$$

$$\sigma_i \sigma_j = \sigma_j \sigma_i = \sigma_{(i+j) \bmod 4}, \quad (3)$$

where $\sigma_i, \sigma_j \in \sigma$, mod indicates modulo operation. Each element in σ represents the orientation information function at a certain layer of network. At the same time, $r = \{r_{\sigma_i}\}$ is defined to represent the orientation information of feature map or convolution kernel, which isomorphisms with σ , viz.,

$$r_{\sigma_i \sigma_j} = r_{\sigma_i} r_{\sigma_j}, \quad (4)$$

where the subscript σ is the index of r . Meanwhile, for any convolution kernel φ and feature map f , we define

$$\sigma_i(\varphi, f) = r_{\sigma_i} \varphi \otimes_{\sigma_i} f, \quad (5)$$

here, \otimes_{σ_i} means the specific convolution mode under σ_i . The reason why \otimes_{σ_i} is designed is that, different hyperparameters in the convolution process, such as stride, padding, and convolution center, easily affect the equivariant acquisition of rotation information. So, to solve this problem as well as ensure the consistency of rotation information acquisition, convolutionally distributive law must be satisfied [20], that is, given a hyperparameter, it satisfies

$$\sigma_i(\varphi, r_{\sigma_i} f) = r_{\sigma_i} \sigma_i \sigma_i^{-1}(\varphi, f). \quad (6)$$

For this goal, it is necessary for us to simultaneously utilize different convolution modes, which details will be given and discussed in the next subsection.

Then, the related operations of group theory are introduced. Since the networks are composed of multiple layers, we naturally represent them using the binary operation of groups. More specifically, we use direct product to represent the extraction of rotation information, and quotient group to represent the compression and fusion of rotation information. Hereinafter, the symbol $\bar{\times}$ and $\bar{/}$ respectively mean the direct product and the quotient group.

Firstly, the group $G_1 = \{\sigma_i | \sigma_i \in \sigma\}$ is used to extract the rotation information from $\{0^\circ, 90^\circ, 180^\circ, 270^\circ\}$ to form the first layer, i.e.,

$$[f_{\sigma_i}^1] = [\sigma_i(\varphi^1, f^1)] = [(r_{\sigma_i} \varphi^1) \otimes_{\sigma_i} f^1], \quad (7)$$

where f^1 and φ^1 respectively represent the input feature map and the convolution kernel of first layer. Subsequently, to make the network have rotation equivariance, two ideas can be easily got. One is to use the symmetric convolution kernel [37], degenerating G_1 to trivial group, i.e., $G_1 \cong \{e\}$. However, this way encounters the issue that the parameter space is smaller and the training is difficult to converge. The other is to use the quotient group to compress the feature information of four orientations, expressed as $G_1 \bar{/} G_1 \cong \{e\}$. But, this idea will cause 4 times the parameter consumption. Considering these, in this paper, we utilize the group direct product $G_2 = \sigma \bar{\times} \sigma = \{(\sigma_j, \sigma_i) | \sigma_j, \sigma_i \in \sigma\}$ to extract the rotation information with the first layer, and the second layer of network is correspondingly designed as

$$\begin{aligned} [(\sigma_j, \sigma_i)(\varphi_{\sigma_j^{-1} \sigma_i}^2, \varphi^1, f^1)] &= [\sigma_j(\varphi_{\sigma_j^{-1} \sigma_i}^2, \sigma_i(\varphi^1, f^1))] \\ &= [(r_{\sigma_j} \varphi_{\sigma_j^{-1} \sigma_i}^2) \otimes_{\sigma_j} (f_{\sigma_i}^1)], \end{aligned} \quad (8)$$

where $\varphi_{\sigma_j^{-1} \sigma_i}^2$ represents the convolution kernels corresponding to the relative orientation information between two layers.

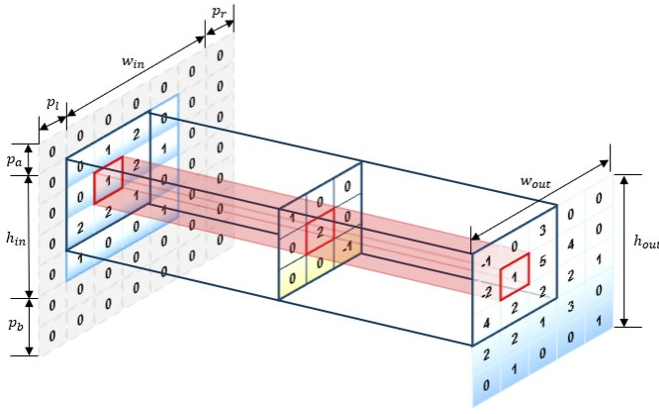


Fig. 2. An example of padding-based convolution process.

Then, to fuse the features of four directions, we use the quotient group to compress Eq. (8). Let $\bar{G}_2 = \{(\sigma_0, \sigma_i) | \sigma_i \in \sigma\}$, the updated second layer will become

$$G_2' = G_2 \bar{G}_2 = \{(\sigma_j, \sigma_0) \bar{G}_2 | \sigma_j \in \sigma\}, \quad (9)$$

$$\begin{aligned} [f_{\sigma_j}^2] &= [(\sigma_j, \sigma_0) \bar{G}_2 (\varphi_{\sigma_j^{-1}\sigma_i}^2, \varphi^1, f^1)] \\ &= \left[\sum_{\sigma_i \in \sigma} (\sigma_j, \sigma_i) (\varphi_{\sigma_j^{-1}\sigma_i}^2, \varphi^1, f^1) \right]. \end{aligned} \quad (10)$$

Obviously, due to $G_1 \cong G_2'$, the second layer $f_{\sigma_j}^2$ can be reused.

At last, in order to obtain the equivariant result, we add the third layer to perform weighted fusion on the feature maps obtained from the second layer. Given the quotient group $G_3 = G_2' \bar{G}_2' \cong \{e\}$, we design

$$f^3 = G_3 (\varphi^3, \varphi_{\sigma_j^{-1}\sigma_i}^2, \varphi^1, f^1) = \sum_{\sigma_j \in \sigma} (r_{\sigma_j} \varphi^3) \otimes_{\sigma_j} (f_{\sigma_j}^2), \quad (11)$$

where φ^3 denotes the convolution kernel of the third layer f^3 .

It should be stressed that, to completely achieve rotation equivariance of network, the three layers $f_{\sigma_i}^1$, $f_{\sigma_j}^2$, and f^3 must be used simultaneously. For the second layer, it can be used in cycles. The detailed proof of the rotation equivariance of this convolution-group framework (i.e., these three layers) are given in Appendix A as well.

C. Padding-based Rotation Equivariant Convolution Mode (PreCM)

In the former subsection, we introduced \otimes_{σ_i} to represent different convolution modes. Hereinafter, a detailed realization scheme is proposed through padding. The reason why we choose padding as the tool is mainly due to that it can make different convolution modes have similar hyperparameters without discarding the original information as much as possible.

In detail, we firstly define the convolution expression with padding as

$$\begin{aligned} (f_{out})_{w_{out} \times h_{out}} &= (\varphi)_{w_{\varphi} \times h_{\varphi}} \otimes_{\sigma_i} (f_{in})_{w_{in} \times h_{in}} \\ &= (\varphi)_{w_{\varphi} \times h_{\varphi}} \otimes [(f_{in})_{w_{in} \times h_{in}} \oplus P_{\sigma_i}], \end{aligned} \quad (12)$$

where f_{out} represents the output feature map, f_{in} means the input feature map, (w_{out}, h_{out}) and (w_{in}, h_{in}) are the width and height of the output and input feature maps, respectively. $(w_{\varphi}, h_{\varphi})$ is the width and height of convolution kernel. The symbol \oplus means the operation of adding padding to the input feature map. P_{σ_i} is the group of padding methods under σ_i , viz., $P_{\sigma_i} = [p_{\sigma_i,a}, p_{\sigma_i,b}, p_{\sigma_i,l}, p_{\sigma_i,r}]$, where $p_{\sigma_i,a}$ is the padding above image, $p_{\sigma_i,b}$ is the padding below image, $p_{\sigma_i,l}$ is the padding on the left, and $p_{\sigma_i,r}$ is the padding on the right. Note that, when $\sigma_i = \sigma_0$, the subscript associated with the convolution mode is omitted. A simple example of padding-based convolution process is shown in Fig. 2.

Then, we further adopt the matrix expansion [38] to make Eq. (12) become the matrix multiplication form, that is,

$$(F_{out})_{w_{out} h_{out} \times 1} = (\Phi)_{w_{out} h_{out} \times w'_{in} h'_{in}} (F_{in})_{w'_{in} h'_{in} \times 1}, \quad (13)$$

where F_{out} , Φ , and F_{in} respectively correspond to the matrix forms of f_{out} , φ , and f_{in} . $w'_{in} = p_l + p_r + w_{in}$, $h'_{in} = p_a + p_b + h_{in}$. The specific transform process is also given in Eq. (14), where m represents the m -th element of the column vector F_{out} , n means the n -th element of the column vector F_{in} , (u, v) denotes the u -th row and v -th column of matrix Φ . (w_s, h_s) is the stride in the directions of width and height, respectively, and (w_d, h_d) are the dilation in the direction of width and height, respectively. $\langle A \rangle$ means the downward rounded result of A and the symbol $\{A/B\}$ is the remainder of A divided by B . Fig. 3 shows a concrete example.

After this, we use the form of matrix multiplication to derive the conditions required for rotation equivariance. Let

$$\begin{aligned} [F_{in}]_t &= \text{flatten}((r_{\sigma_t} f_{in}) \oplus P_{\sigma_t}), \\ [F_{out}]_t &= \text{flatten}(r_{\sigma_t} f_{out}), \\ [\Phi]_t &= \text{sparse}(r_{\sigma_t} \varphi), \end{aligned} \quad (15)$$

where $\sigma_t \in \sigma$. Then, Eq. (6) can be rewritten as

$$\begin{aligned} \sigma_i(\varphi, r_{\sigma_t} f) &= r_{\sigma_t} \sigma_i \sigma_t^{-1}(\varphi, f) \\ &\Rightarrow r_{\sigma_i} \varphi \otimes_{\sigma_i} r_{\sigma_t} f = r_{\sigma_t} (r_{\sigma_i \sigma_t^{-1}} \varphi \otimes_{\sigma_i \sigma_t^{-1}} f) \\ &\stackrel{i \equiv t}{\Rightarrow} r_{\sigma_t} \varphi \otimes_{\sigma_t} r_{\sigma_t} f = r_{\sigma_t} (\varphi \otimes_{\sigma_0} f) \\ &\Rightarrow [\phi]_t [F_{in}]_t = [F_{out}]_t, \end{aligned} \quad (16)$$

where $[F_{out}]_t$ is the result of flattening the output feature map after r_{σ_t} (i.e., a column vector). Thus, there has a row transformation relationship between $[F_{out}]_t$ and $[F_{out}]$. Eq. (17) shows the detailed process, wherein $R_{t,out}$ represents the row transformation function between $[F_{out}]_t$ and $[F_{out}]$ under σ_t . Further, we use the matrix form of convolution to describe Eq. (17), and obtain

$$\begin{aligned} [F_{out}]_t(m) &= F_{out}(R_{t,out}(m)) \\ &= \sum_{n=0}^{h_{out} w_{out} - 1} \Phi(R_{t,out}(m), n) F_{in}(n) \\ &= \sum_{n=0}^{h_{out} w_{out} - 1} \Phi(R_{t,out}(m), R_{t,in}(n)) F_{in}(R_{t,in}(n)), \end{aligned} \quad (18)$$

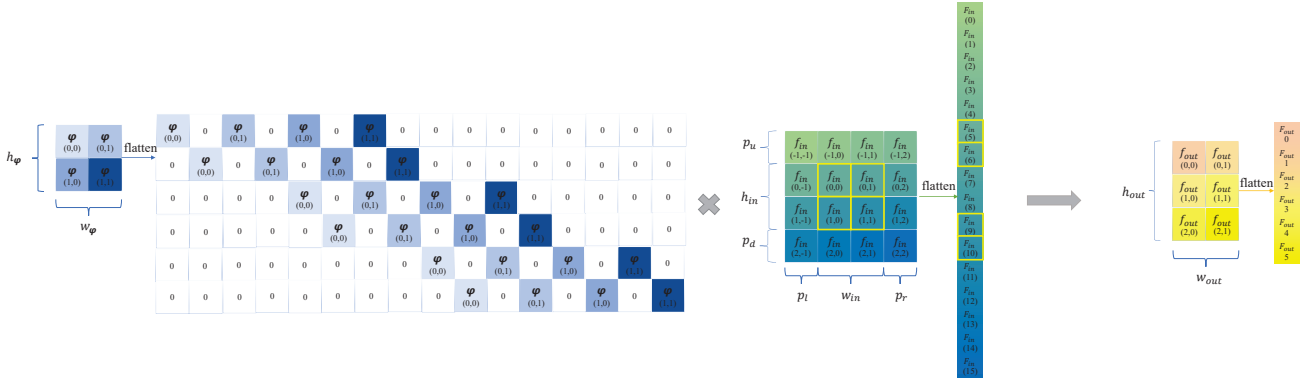


Fig. 3. An example of convolution in flatten form.

$$\begin{aligned}
 F_{out}(m) &= \text{flatten}(f_{out})(m) := f_{out}(\langle m/w_{out} \rangle, \{m/w_{out}\}), \\
 F_{in}(n) &= \text{flatten}(f_{in} \oplus p_a, p_b, p_l, p_r)(n) := f_{in}(\langle n/w'_{in} \rangle - p_a, \{n/w'_{in}\} - p_l), \\
 \Phi(u, v) &= \text{sparse}(\varphi)(u, v) := \varphi\left(\frac{\langle v/w'_{in} \rangle - \langle u/w_{out} \rangle h_s}{h_d}, \frac{\{v/w'_{in}\} - \{u/w_{out}\} w_s}{w_d}\right), \\
 m &= 0, 1, 2, \dots, w_{out}h_{out} - 1, n = 0, 1, 2, \dots, h'_{in}w'_{in} - 1, u = 0, 1, 2, \dots, w_{out}h_{out} - 1, v = 0, 1, 2, \dots, h'_{in}w'_{in} - 1.
 \end{aligned} \tag{14}$$

$$\begin{aligned}
 [F_{out}]_t(m) &= F_{out}(R_{t,out}(m)), \\
 R_{t,out}(m) &= \begin{bmatrix} w_{out} & 1 \end{bmatrix} \left(\begin{bmatrix} \cos \frac{\pi t}{2} & \sin \frac{\pi t}{2} \\ -\sin \frac{\pi t}{2} & \cos \frac{\pi t}{2} \end{bmatrix} \begin{bmatrix} \langle m/w_{\sigma_t,out} \rangle - \frac{h_{\sigma_t,out}-1}{2} \\ \{m/w_{\sigma_t,out}\} - \frac{w_{\sigma_t,out}-1}{2} \end{bmatrix} + \begin{bmatrix} \frac{h_{\sigma_t,out}-1}{2} \\ \frac{w_{\sigma_t,out}-1}{2} \end{bmatrix} \right).
 \end{aligned} \tag{17}$$

$$\begin{aligned}
 ([\phi]_t[F_{in}]_t)(m) &= \sum_{n=0}^{h_{\sigma_t,out}w_{\sigma_t,out}-1} [\phi]_t(m, n)[F_{in}]_t(n) = \sum_{n=0}^{h_{\sigma_t,out}w_{\sigma_t,out}-1} \Phi(R_{t,\varphi}(m, n))[F_{in}]_t(n), \\
 R_{t,\varphi}(m, n) &= \left(\begin{bmatrix} \cos \frac{\pi t}{2} & \sin \frac{\pi t}{2} \\ -\sin \frac{\pi t}{2} & \cos \frac{\pi t}{2} \end{bmatrix} \begin{bmatrix} \frac{1}{h_{\sigma_t,d}} (\langle n/w_{\sigma_t,in} \rangle - \langle m/w_{\sigma_t,out} \rangle h_{\sigma_t,s}) - \frac{h_{\sigma_t,\varphi}-1}{2} \\ \frac{1}{w_{\sigma_t,d}} (\{n/w_{\sigma_t,in}\} - \{m/w_{\sigma_t,out}\} w_{\sigma_t,s}) - \frac{w_{\sigma_t,\varphi}-1}{2} \end{bmatrix} + \begin{bmatrix} \frac{h_{\sigma_t,\varphi}-1}{2} \\ \frac{w_{\sigma_t,\varphi}-1}{2} \end{bmatrix} \right).
 \end{aligned} \tag{19}$$

where $F_{in}(R_{t,in}(n)) = \text{flatten}(r_{\sigma_t} f'_{in})(n)$.

For $[\phi]_t[F_{in}]_t$, it can be recast as Eq. (19), where $w_{\sigma_t,*}$ represents hyperparameters related to the size of feature map and the convolution under σ_t . $(w_{\sigma_t,\phi}, h_{\sigma_t,\phi})$ represents the width and height of the convolution kernel after rotating r_{σ_t} , respectively. Comparing Eqs. (18) and (19), we can easily get

$$\begin{aligned}
 [F_{in}]_t(n) &= F_{in}(R_{t,in}(n)), \\
 h_{out}w_{out} &= h_{\sigma_t,out}w_{\sigma_t,out}, \\
 \Phi(R_{t,out}(m), R_{t,in}(n)) &= \Phi(R_{t,\varphi}(m, n)).
 \end{aligned} \tag{20}$$

After further derivations, the following conclusions can be attained as well, i.e.,

$$\begin{aligned}
 w_{out} &= (p_l + p_r + w_{in} - w_d(w_\varphi - 1) - 1)/w_s + 1, \\
 h_{out} &= (p_a + p_b + h_{in} - h_d(h_\varphi - 1) - 1)/h_s + 1,
 \end{aligned} \tag{21a}$$

$$\begin{bmatrix} p_{\sigma_t,a} \\ p_{\sigma_t,l} \\ p_{\sigma_t,b} \\ p_{\sigma_t,r} \end{bmatrix} = \begin{bmatrix} 0 & 0 & 0 & 1 \\ 1 & 0 & 0 & 0 \\ 0 & 1 & 0 & 0 \\ 0 & 0 & 1 & 0 \end{bmatrix}^t \begin{bmatrix} p_a \\ p_l \\ p_b \\ p_r \end{bmatrix}. \tag{21b}$$

Note that, the detailed deductions of Eqs. (21a) and (21b) are respectively presented in Appendixes B and C.

So far, a concrete padding-based rotation equivariant mode has been given. Meanwhile, we emphasize that there are many ways to realize Eq. (21a), and researchers are free to set its hyperparameters according to practical need, but here we recommend using Eq. (22), which can avoid unnecessary

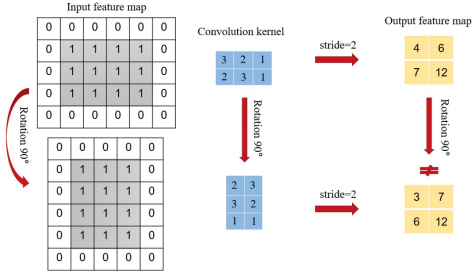


Fig. 4. An example of the limitation of existing rotation equivariance.

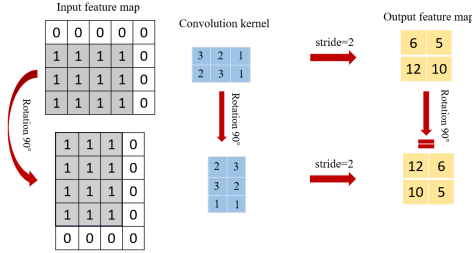


Fig. 5. An example of the rotation equivariance of PreCM.

padding as well as satisfy Eq. (21a).

$$\begin{aligned}
 p_a &= p_{ab} - p_b, \\
 p_r &= p_{rl} - p_l, \\
 p_b &= \langle p_{ab} | 2 \rangle, \\
 p_l &= \langle p_{rl} | 2 \rangle, \\
 p_{ab} &= (h_{out} - 1) h_s + h_d (h_\varphi - 1) + 1 - h_{in}, \\
 p_{rl} &= (w_{out} - 1) w_s + w_d (w_\varphi - 1) + 1 - w_{in}.
 \end{aligned} \tag{22}$$

To sum up, in this subsection, we use padding to design a specific convolutional mode to achieve rotation equivariance. The most significant advantage of this mode is that it can avoid the influence of network hyperparameters on rotation equivariance, thereby extending the rotation equivariance to a wider range of applications.

D. Characteristic Analysis of PreCM

As mentioned earlier, to achieve rotation equivariance in networks, the convolutionally distributive law (Eq. (6)) must hold for images and convolutional kernels of arbitrary sizes. Let us illustrate this point with a specific example. Suppose $i = t = 1$, then Eq. (6) can be written as:

$$\sigma_1(\varphi, r_{\sigma_1} f) = r_{\sigma_1} \varphi \otimes_{\sigma_1} (r_{\sigma_1} f) = r_{\sigma_1} (\varphi \otimes_{\sigma_0} f). \tag{23}$$

In terms of the studies on rotation equivariance, the design of equivariance is usually limited by convolutionally distributive law, making them unable to be applied to images and convolutional kernels of arbitrary size, thereby limiting their applications [20]. A concrete example is shown in Fig. 4, where the image size $w_{in} \times h_{in} = 4 \times 3$, $w_{out} \times h_{out} = 2 \times 2$, convolution kernel size $w_\varphi \times h_\varphi = 3 \times 2$, and dilation $w_d \times h_d = 1 \times 1$, stride $w_s \times h_s = 2 \times 2$, padding $p_a = p_b = p_r = p_l = 1$. It can be seen that convolutionally distributive law is not successfully implemented under this design. However, for our

proposed convolution mode, it effectively solves this problem. That is, from Eq. (22), researchers can calculate the required padding based on the given size of input images, the required sizes of output images and convolution kernels as well as the hyperparameters of network such as dilation and stride, to achieve the rotation equivariance of network. For further demonstrating this point, we here also take the parameters given in Fig. 4 as an example. Using Eq. (22), one can get $p_a = 1, p_r = 1, p_b = 0, p_l = 0$. So, with these values, once we change the convolution mode of Fig. 4, we can easily realize the convolutionally distributive law in Fig. 5.

In conclusion, the proposed PreCM is regardless of the parameters and can be directly used as a replacement component to replace the convolution operations in existing networks. Therefore, to some extent, it can also be seen as one plug-and-play multi-scale rotation equivariant convolution. The whole framework of PreCM is displayed in Fig. 6.

IV. EXPERIMENTS

In this section, we first introduce the training setup and the datasets Satellite Images of Water Bodies [39], DRIVE [40], and Floodnet [41] that respectively represents the binary, small-sample, and multi-class segmentation tasks. Then, the evaluation metrics are introduced. Finally, we apply PreCM as a replacement component to different semantic segmentation networks for evaluating its performance.

A. Training Setup and Datasets

1) *Training Setup*: During the training process, we used the Adam optimizer to update the training of 150 epochs with a batch size of 4. The learning rate was 0.0001 and the weight attenuation coefficient was 0.0005. All of our experiments were performed on a desktop PC equipped with NVIDIA GeForce RTX 4090 and 64 GB RAM. In order to reduce the uncertainty caused by randomness and ensure reliability of the results, we repeat experiments ten times.

2) *Satellite Images of Water Bodies*: This dataset is a set of water body images taken by the Sentinel-2 satellite from any angle, which belongs to the category of binary semantic segmentation dataset. Each image is accompanied by a black and white mask, in which white represents water body and black represents something other than water. These masks are generated by calculating the normalized water difference index (NDWI) [42]. This dataset contains 2328 images, of which 1,862 were used for training and 466 for testing.

3) *DRIVE*: Within the binary semantic segmentation task, there also exist some other datasets, e.g., the medical image datasets that we often cannot obtain enough data for training. So, to test the performance of PreCM in the semantic segmentation of small-sample, the dataset DRIVE (Digital Retinal Images for Vessel Extraction) [40] is chosen as the second dataset. It is attained from a diabetic retinopathy screening program in the Netherlands, composed of a total of JPEG 40 color fundus images. These images were equally divided into 20 images for training and 20 images for testing.

4) *Floodnet*: In addition to binary semantic segmentation, multi-class semantic segmentation with relatively complex

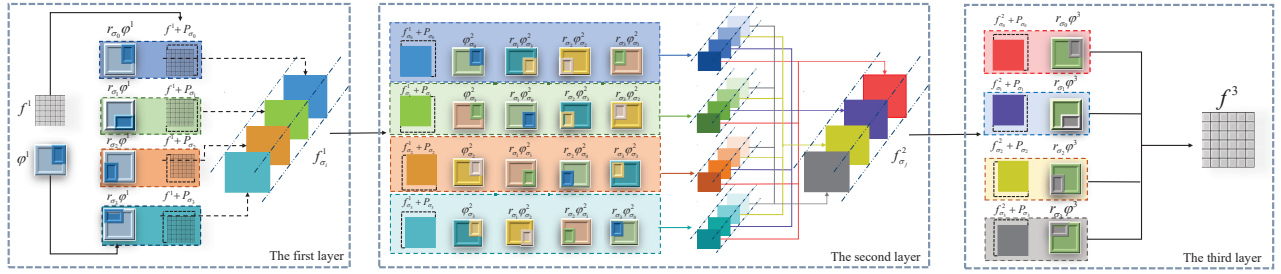


Fig. 6. The whole framework of PreCM.

tasks is also one important branch in semantic segmentation family. To evaluate the performance of PreCM in this aspect, we here choose the dataset Floodnet [41] as the final experimental data. It is divided into ten categories, including background, building-flooded, building-non-flooded, road-flooded, road-non-flooded, water, tree, vehicle, pool, grass, and contains 1445 images, of which 1120 were used for training and 325 for testing.

B. Evaluation Metrics

In this paper, the metrics Intersection Over Union (IOU), Mean Intersection over Union (MIOU), and Dice Similarity Coefficient (DICE) are adopted to evaluate the segmentation results of networks [43], which are respectively defined as

$$\begin{aligned} IOU &= \frac{TP}{TP + FN + FP}, \\ MIOU &= \frac{1}{2} \left(\frac{TP}{TP + FN + FP} + \frac{TN}{TN + FN + FP} \right), \\ DICE &= \frac{2TP}{2TP + FP + FN}, \end{aligned} \quad (24)$$

where TP is the number of positive examples predicted correctly, FP means the number of positive examples prediction errors, TN represents the number of negative examples predicted correctly, and FN denotes the number of negative examples prediction errors.

In addition, to measure the changes of predicted pixels before and after rotation, a new metric rotation difference (RD) is also proposed here, which definition is

$$RD = \frac{|f_{r_{\sigma_i}} - f_{r_{\sigma_0}}|}{w_{out} \times h_{out}}, \quad (25)$$

where w_{out}, h_{out} represent the width and height of the output feature map respectively. $f_{r_{\sigma_i}}$ means the corresponding output feature map when the test maps are rotated r_{σ_i} . In this paper, $r_{\sigma_i} = \{r_{\sigma_0}, r_{\sigma_1}, r_{\sigma_2}, r_{\sigma_3}\} = \{0^\circ, 90^\circ, 180^\circ, 270^\circ\}$.

C. Experimental Results

Three classical semantic segmentation networks: U-net [25], SegNet [26], PSPNet [27], and three lightweight semantic segmentation networks: Enet [29], Erfnet [30], BiSeNetV2 [31] are selected as the baselines to test the performance of PreCM. It should be pointed out that, these networks are

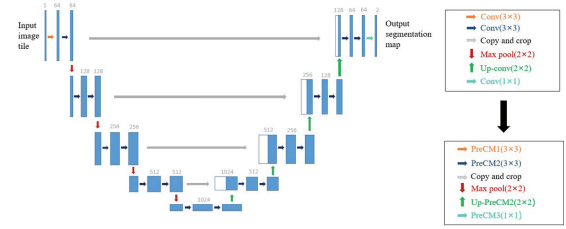


Fig. 7. The replacement process of U-net with PreCM. PreCM1 is the first layer of PreCM, PreCM2 represents the second layer of PreCM, and PreCM3 denotes the third layer of PreCM.

original networks without pre-training. In order to achieve rotation equivariance, we replace the first convolution layer of these networks with the first layer of PreCM, and the last convolution layer of these networks with the third layer of PreCM. The remaining convolution layers are replaced by the second layer of PreCM. Taking U-net as an example, Fig. 7 correspondingly shows its PreCM replacement process. Note that, our proposed PreCM requires that the number of channels in each layer need to be reduced by half so as to keep the number of parameters roughly the same.

1) *Satellite Images of Water Bodies*: Table I shows the evaluation results of six networks before and after the PreCM replacement. From it, three points can be easily obtained. The first one is that, the proposed PreCM takes into account different orientation information of images, so when the test images are not rotated, the networks with PreCM still have significant improvements in the evaluation metrics. The second one is that, because the PreCM-based networks have rotation equivariance, the metrics' values do not change when the test images are rotated $90^\circ/180^\circ/270^\circ$, and RD values are always 0. In contrast, the orientation information of original networks can only be obtained from the dataset itself. So, without the images with different orientation angles, the IOU, MIOU, and DICE values of original networks decrease after rotating the test images. The value of RD also shows that when the images are rotated, the segmentation results are different from the original output feature maps, resulting in poor universality. The last point is that, all the original six networks contain up-sampling and down-sampling as well as some special design of convolution, such as dilated convolution, transposed convolution, variable stride convolution, and flattened convolution. Therefore, the successful application

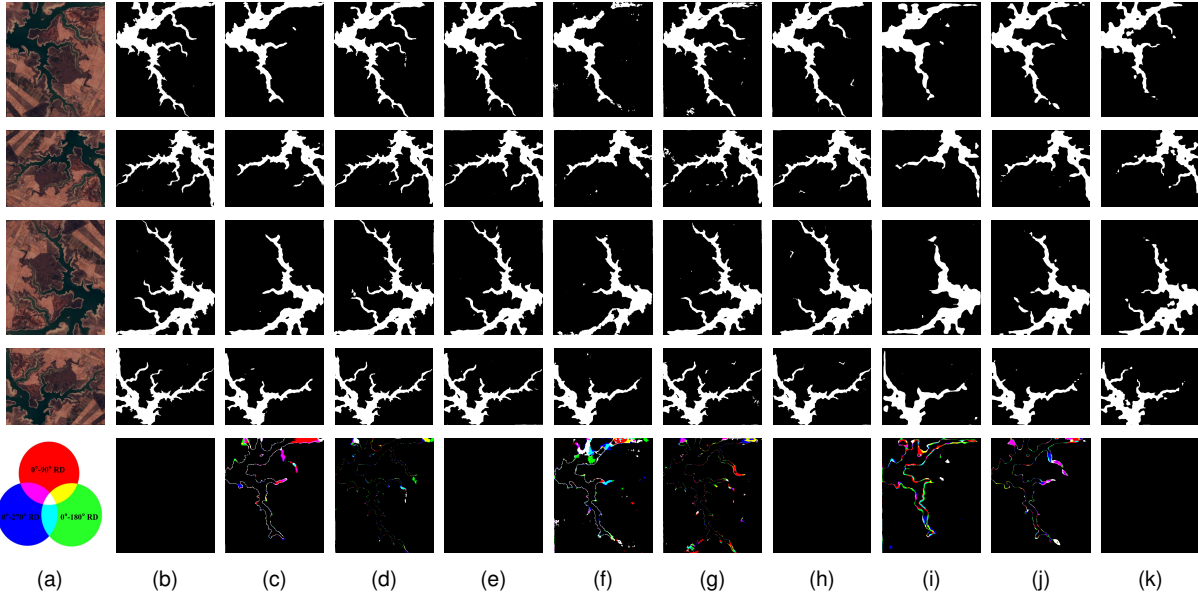


Fig. 8. Visualization results of classical semantic segmentation networks on Satellite Images of Water Bodies. (a) Raw optical image; (b) Ground Truth; (c) U-net; (d) U-net+aug; (e) U-net(PreCM); (f) SegNet; (g) SegNet+aug; (h) SegNet(PreCM); (i) PSPNet; (j) PSPNet+aug; (k) PSPNet(PreCM). The last row are the difference maps, wherein red, green, and blue respectively denote the rotation difference between 0° and 90° , 0° and 180° , 0° and 270° .

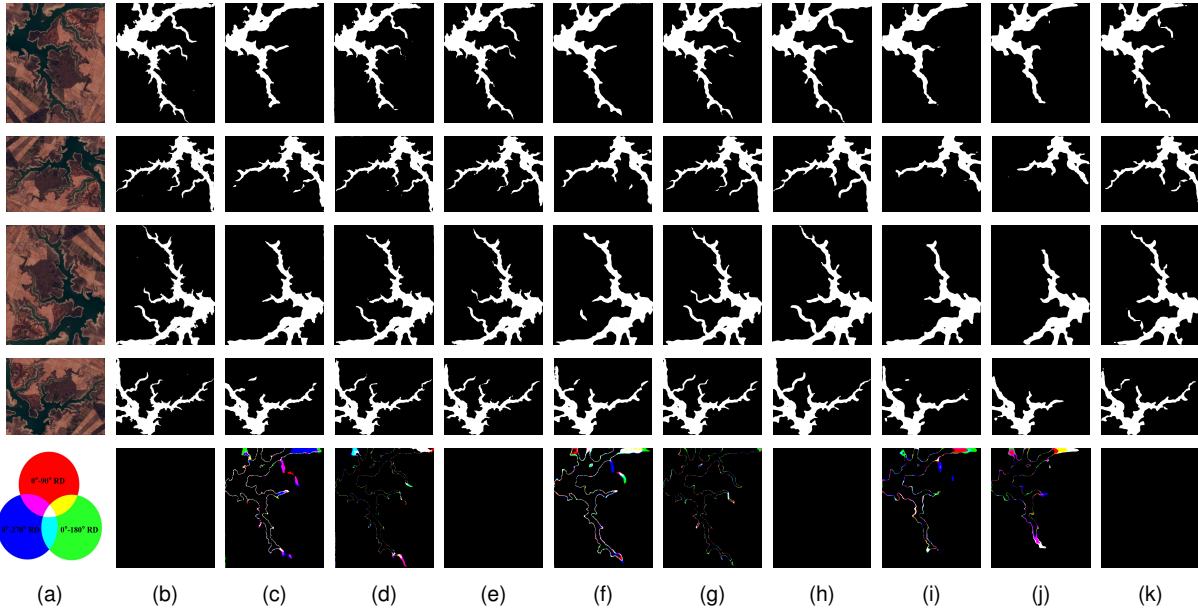


Fig. 9. Visualization results of lightweight semantic segmentation networks on Satellite Images of Water Bodies. (a) Raw optical image; (b) Ground Truth; (c) Enet; (d) Enet+aug; (e) Enet(PreCM); (f) Erfnet; (g) Erfnet+aug; (h) Erfnet(PreCM); (i) BisenetV2; (j) BisenetV2+aug; (k) BisenetV2(PreCM). The last row are the difference maps, wherein red, green, and blue respectively denote the rotation difference between 0° and 90° , 0° and 180° , 0° and 270° .

directly proves the universality of PreCM for arbitrarily sized images and convolution kernels. Indirectly, this also verifies the correctness of our mathematical deductions.

As is well-known, data augmentation technology can allow the network to learn the rotation features well from objects with different orientations. Here, to demonstrate the comparability of PreCM with data augmentation, we do the following experiments, wherein the data augmentation expands the dataset by a factor of three, including rotation 90° , 180° , and 270° . The quantitative results are correspondingly shown

in Table II. From it, one can find that for most networks, the IOU, MIOU, and DICE values obtained by the PreCM-based networks are slightly better than the data augmentation-based networks. However, in terms of RD, the values of data augmentation are all higher than the PreCM-based networks, which shows that even though data augmentation improves the segmentation accuracy of networks, it still does not resolve the differences caused by image rotation. Besides, the amount of data used in the PreCM-based networks is not increased. So, the training time of these networks is much less than

TABLE I
EVALUATION RESULTS ON SATELLITE IMAGES OF WATER BODIES, FLOODNET DATASETS AND DRIVE.

Network	Rotation	Satellite Images of Water Bodies				DRIVE				Floodnet			
		IOU	MIOU	DICE	RD(%)	IOU	MIOU	DICE	RD(%)	IOU	MIOU	DICE	RD(%)
U-net	0°	0.8088	0.8682	0.8873		0.6687	0.8169	0.8010		0.7769	0.8731	0.8581	
	90°	0.7947	0.8581	0.8776	3.9545	0.6336	0.7975	0.7752	2.2307	0.7141	0.8369	0.8119	14.7176
	180°	0.7954	0.8591	0.8782	3.5765	0.6385	0.8000	0.7789	2.1451	0.7400	0.8519	0.8306	12.5696
	270°	0.7944	0.8577	0.8779	3.9198	0.6344	0.7977	0.7758	2.0732	0.7149	0.8373	0.8117	14.7350
U-net(PreCM)	0°/90°/180°/270°	0.8490	0.8960	0.9150	0.0000	0.6955	0.8316	0.8201	0.0000	0.7893	0.8804	0.8672	0.0000
SegNet	0°	0.7751	0.8479	0.8609		0.5058	0.7280	0.6707		0.6979	0.8276	0.8006	
	90°	0.7615	0.8390	0.8509	3.9880	0.4582	0.7020	0.6272	3.1492	0.6266	0.7862	0.7448	21.6232
	180°	0.7642	0.8404	0.8524	3.6779	0.4709	0.7088	0.6392	3.1589	0.6665	0.8093	0.7757	18.4317
	270°	0.7582	0.8362	0.8490	3.9265	0.4751	0.7114	0.6431	3.2096	0.6260	0.7859	0.7451	21.7578
Segnet(PreCM)	0°/90°/180°/270°	0.8455	0.8956	0.9124	0.0000	0.6257	0.7931	0.7694	0.0000	0.7442	0.8544	0.8347	0.0000
PSPNet	0°	0.7179	0.8105	0.8210		0.3664	0.6487	0.5351		0.7704	0.8693	0.8521	
	90°	0.7100	0.8036	0.8144	2.4610	0.3517	0.6407	0.5194	2.2951	0.7141	0.8369	0.8128	15.4306
	180°	0.7151	0.8105	0.8210	2.3109	0.3528	0.6413	0.5206	2.2898	0.7393	0.8510	0.8243	13.0140
	270°	0.7110	0.8045	0.8155	2.4094	0.3537	0.6418	0.5219	2.1921	0.7236	0.8426	0.8212	14.7735
PSPNet(PreCM)	0°/90°/180°/270°	0.7803	0.8522	0.8650	0.0000	0.4045	0.6675	0.5753	0.0000	0.7746	0.8716	0.8529	0.0000
ENet	0°	0.8396	0.8916	0.9078		0.6029	0.7799	0.7518		0.7979	0.8852	0.8721	
	90°	0.8275	0.8842	0.8994	2.8088	0.5761	0.7652	0.7307	3.0391	0.7321	0.8471	0.8226	14.3431
	180°	0.8294	0.8851	0.9005	2.7008	0.5801	0.7673	0.7337	2.9412	0.7515	0.8584	0.8381	13.1061
	270°	0.8258	0.8826	0.8992	2.7887	0.5752	0.7645	0.7299	2.9972	0.7422	0.8530	0.8314	13.7670
Enet(PreCM)	0°/90°/180°/270°	0.8759	0.9168	0.9307	0.0000	0.6462	0.8042	0.7848	0.0000	0.8041	0.8886	0.8748	0.0000
Erfnet	0°	0.8313	0.8865	0.9018		0.5554	0.7542	0.7133		0.7965	0.8844	0.8713	
	90°	0.8112	0.8726	0.8874	3.1766	0.5259	0.7378	0.6882	3.1676	0.7286	0.8452	0.8218	14.5658
	180°	0.8245	0.8814	0.8964	2.7502	0.5419	0.7465	0.7020	2.8808	0.7639	0.8655	0.8463	11.9732
	270°	0.8191	0.8784	0.8935	2.9893	0.5270	0.7383	0.6891	3.0653	0.7304	0.8463	0.8236	14.0421
Erfnet(PreCM)	0°/90°/180°/270°	0.8628	0.9087	0.9225	0.0000	0.6564	0.8096	0.7923	0.0000	0.8149	0.8947	0.8815	0.0000
BiSeNetV2	0°	0.7903	0.8598	0.8737		0.3553	0.6418	0.5231		0.7733	0.8712	0.8563	
	90°	0.7792	0.8519	0.8657	3.2308	0.3046	0.6166	0.4663	2.5874	0.6976	0.8272	0.7973	16.4675
	180°	0.7786	0.8523	0.8650	2.9393	0.3228	0.6263	0.4874	2.4878	0.7202	0.8404	0.8157	14.2976
	270°	0.7818	0.8537	0.8672	3.0281	0.2974	0.6128	0.4578	2.5267	0.7041	0.8310	0.8033	16.0286
BiSeNetV2(PreCM)	0°/90°/180°/270°	0.8263	0.8833	0.8987	0.0000	0.4045	0.6675	0.5753	0.0000	0.7992	0.8859	0.8724	0.0000

TABLE II
COMPARISON OF DATA AUGMENTATION AND PRECM REPLACEMENT.

Network	Satellite Images of Water Bodies				DRIVE				Floodnet				Average			
	IOU	MIOU	DICE	RD(%)	IOU	MIOU	DICE	RD(%)	IOU	MIOU	DICE	RD(%)	IOU	MIOU	DICE	RD(%)
U-net+aug	0.8447	0.8944	0.9110	2.6510	0.7026	0.8354	0.8250	0.7949	0.7870	0.8789	0.8644	3.9303	0.7781	0.8695	0.8668	2.4587
U-net(PreCM)	0.8490	0.8960	0.9150	0.0000	0.6955	0.8316	0.8201	0.0000	0.7893	0.8804	0.8672	0.0000	0.7780	0.8693	0.8674	0.0000
SegNet+aug	0.8438	0.8950	0.9107	2.9412	0.5820	0.7698	0.7339	2.1960	0.7415	0.8526	0.8307	10.4956	0.7224	0.8391	0.8251	5.2109
SegNet(PreCM)	0.8455	0.8956	0.9124	0.0000	0.6257	0.7931	0.7694	0.0000	0.7442	0.8544	0.8347	0.0000	0.7385	0.8477	0.8388	0.0000
PSPNet+aug	0.7970	0.8655	0.8717	1.6843	0.3905	0.6615	0.5612	2.1496	0.7879	0.8792	0.8625	6.1894	0.6584	0.8021	0.7644	3.3411
PSPNet(PreCM)	0.7803	0.8522	0.8650	0.0000	0.4045	0.6675	0.5753	0.0000	0.7746	0.8716	0.8529	0.0000	0.6531	0.7971	0.7644	0.0000
Enet+aug	0.8705	0.9140	0.9261	1.7746	0.6304	0.7949	0.7729	2.3634	0.8029	0.8877	0.8715	4.8200	0.7679	0.8655	0.8568	2.9860
Enet(PreCM)	0.8759	0.9168	0.9307	0.0000	0.6462	0.8042	0.7848	0.0000	0.8041	0.8886	0.8748	0.0000	0.7754	0.8699	0.8634	0.0000
Erfnet+aug	0.8571	0.9055	0.9176	1.9041	0.6318	0.7958	0.7740	2.1009	0.8038	0.8882	0.8719	5.9766	0.7642	0.8632	0.8545	3.3272
Erfnet(PreCM)	0.8628	0.9087	0.9225	0.0000	0.6564	0.8096	0.7923	0.0000	0.8149	0.8947	0.8815	0.0000	0.7780	0.8710	0.8712	0.0000
BiSeNetV2+aug	0.7973	0.8700	0.8743	2.1396	0.3851	0.6589	0.5554	2.0553	0.7927	0.8824	0.8707	6.1242	0.6535	0.7996	0.7647	3.4397
BiSeNetV2(PreCM)	0.8263	0.8833	0.8987	0.0000	0.4045	0.6675	0.5753	0.0000	0.7992	0.8859	0.8724	0.0000	0.6767	0.8122	0.7821	0.0000

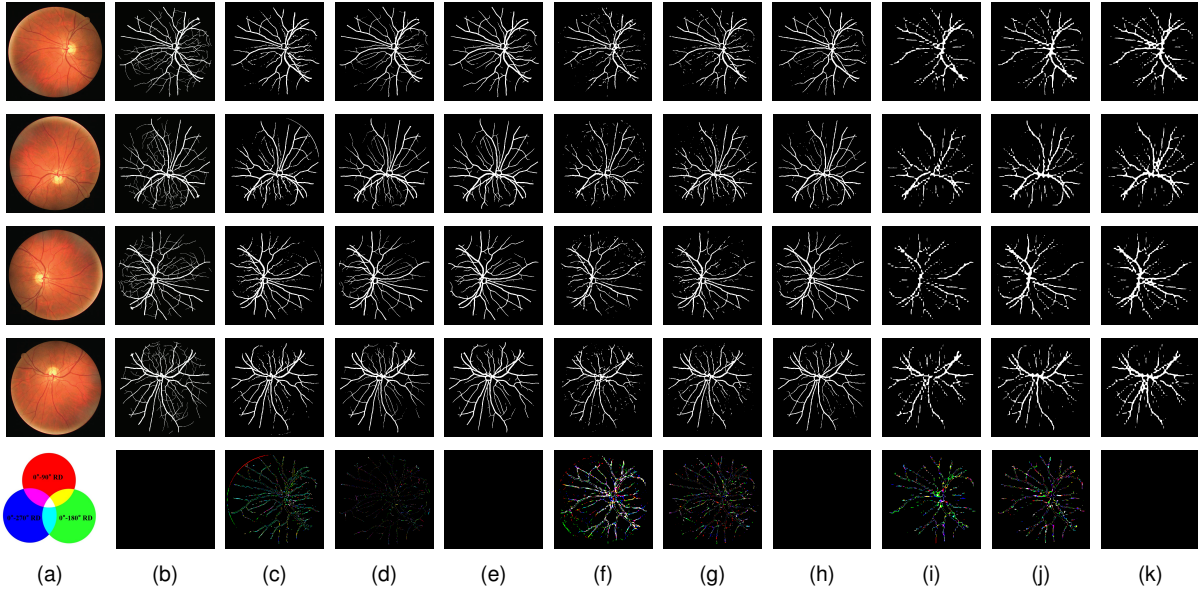


Fig. 10. Visualization results of classical semantic segmentation networks on DRIVE. (a) Raw optical image; (b) Ground Truth; (c) U-net; (d) U-net+aug; (e) U-net(PreCM); (f) SegNet; (g) SegNet+aug; (h) SegNet(PreCM); (i) PSPNet; (j) PSPNet+aug; (k) PSPNet(PreCM). The last row are the difference maps, wherein red, green, and blue respectively denote the rotation difference between 0° and 90° , 0° and 180° , 0° and 270° .

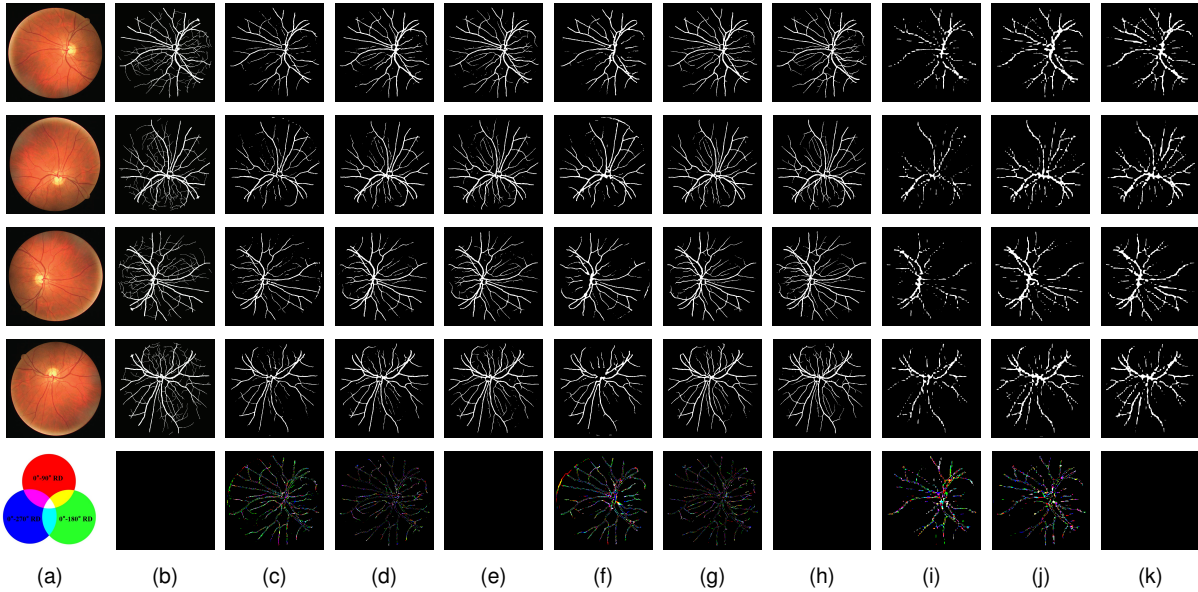


Fig. 11. Visualization results of lightweight semantic segmentation networks on DRIVE. (a) Raw optical image; (b) Ground Truth; (c) Enet; (d) Enet+aug; (e) Enet(PreCM); (f) Erfnet; (g) Erfnet+aug; (h) Erfnet(PreCM); (i) BisenetV2; (j) BisenetV2+aug; (k) BisenetV2(PreCM). The last row are the difference maps, wherein red, green, and blue respectively denote the rotation difference between 0° and 90° , 0° and 180° , 0° and 270° .

that of the data augmentation-based networks. In a nutshell, PreCM exhibits a better overall performance than the data augmentation technology on this dataset.

Also, to visually verify the effectiveness of PreCM, the output feature maps respectively corresponding to 0° , 90° , 180° , and 270° as well as the difference maps including the rotation differences between 0° and 90° (red), 0° and 180° (green), and 0° and 270° (blue) are shown in Figs. 8 and 9. It can be seen that when the test images are rotated, the output feature maps of original networks are really different. In contrast, the data augmentation-based networks can get better segmentation

results, yet there are still some variable pixels in difference maps. However, the PreCM-based networks proposed by us can not only obtain good segmentation results, but also have rotation equivariance, since the feature maps are completely consistent in the four angles $\{0^\circ, 90^\circ, 180^\circ, 270^\circ\}$. The same conclusion can be attained by their corresponding difference maps that are all black in the last row.

2) *DRIVE*: The quantitative results of this dataset are also listed in Tables I and II. It can be seen from Table I, although the training sample has only 20 images, the PreCM-based segmentation networks still perform better than original

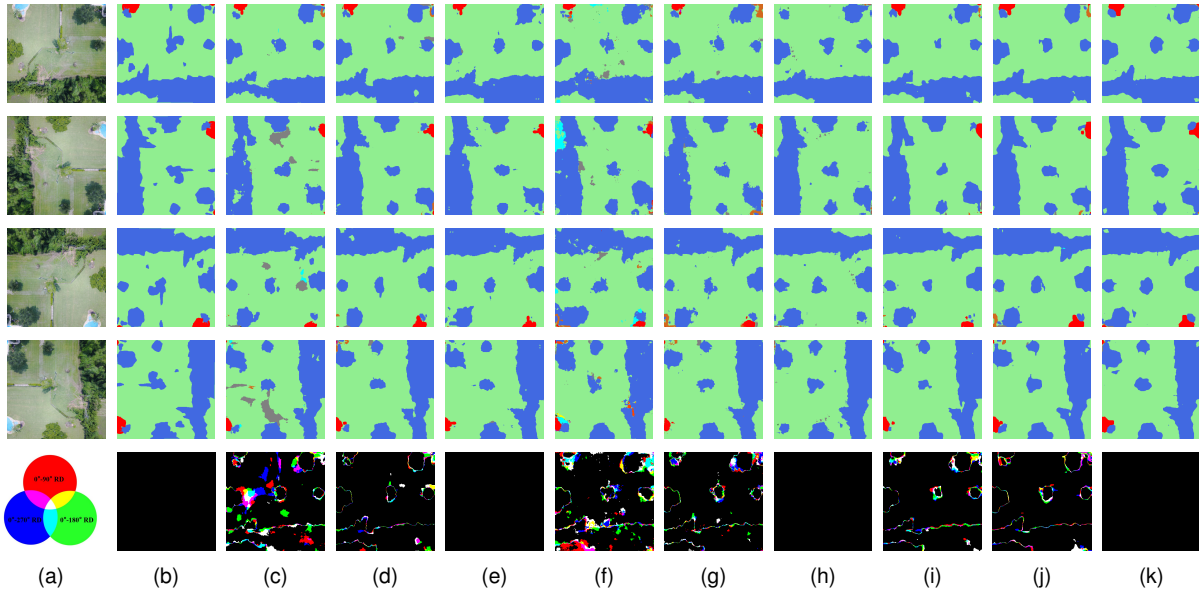


Fig. 12. Visualization results of classical semantic segmentation networks on Floodnet. (a) Raw optical image; (b) Ground Truth; (c) U-net; (d) U-net+aug; (e) U-net(PreCM); (f) SegNet; (g) SegNet+aug; (h) SegNet(PreCM); (i) PSPNet; (j) PSPNet+aug; (k) PSPNet(PreCM). The last row are the difference maps, wherein red, green, and blue respectively denote the rotation difference between 0° and 90° , 0° and 180° , 0° and 270° .

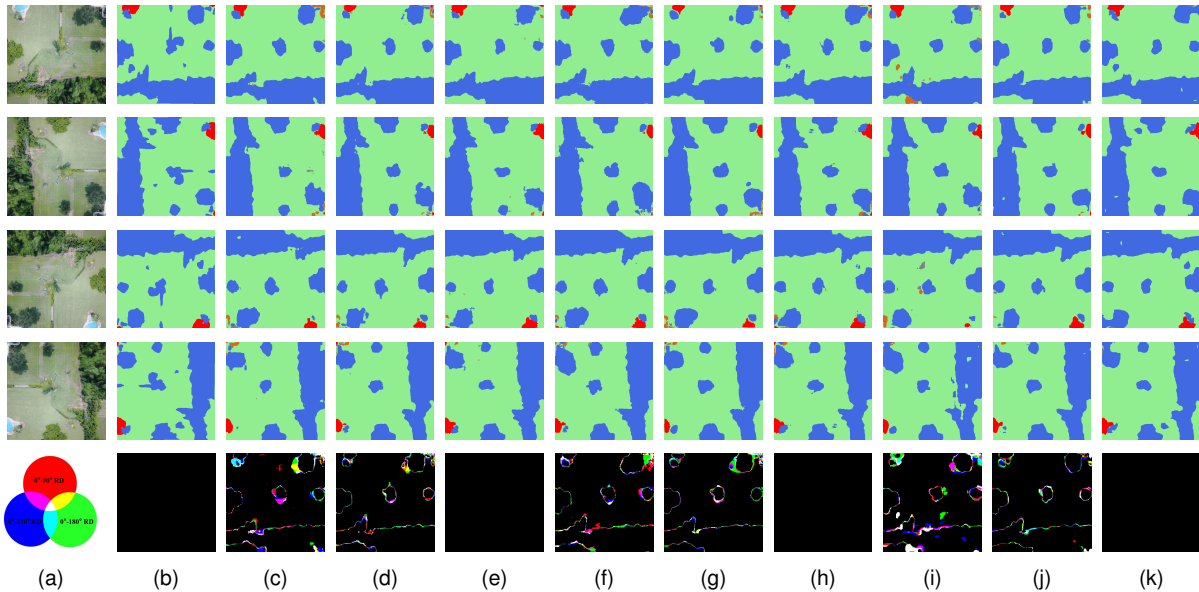


Fig. 13. Visualization results of lightweight semantic segmentation networks on Floodnet. (a) Raw optical image; (b) Ground Truth; (c) Enet; (d) Enet+aug; (e) Enet(PreCM); (f) Erfnet; (g) Erfnet+aug; (h) Erfnet(PreCM); (i) BisenetV2; (j) BisenetV2+aug; (k) BisenetV2(PreCM). The last row are the difference maps, wherein red, green, and blue respectively denote the rotation difference between 0° and 90° , 0° and 180° , 0° and 270° .

networks in the case of 0° . However, once the test images are rotated 90° , 180° , or 270° , the performance of original networks decrease dramatically. Contrastively, the results of the segmentation networks after PreCM replacement remain unchanged. Therefore, the math-driven module PreCM is verified to have a stable rotation equivariance. From Table II, one can find that with a small amount of data, the PreCM-based networks still have great advantages over the data augmentation-based networks, which is specifically reflected in the comparable segmentation results, the improvement of RD, and the reduction of training samples.

Figs. 10 and 11 show some visual results of these segmentation networks. It is easily found that, for original networks and data augmentation-based networks, the results of 90° , 180° , and 270° are inconsistent with the result of 0° , i.e., not rotation equivariant, which can be further verified by the last row. In contrast, the segmented pixels obtained by PreCM-based networks are consistent for these four angles. So, their difference maps are all black. As a result, our proposed replacement component PreCM has greater prospects and advantages.

3) *Floodnet*: From Table I, it can be found that, compared

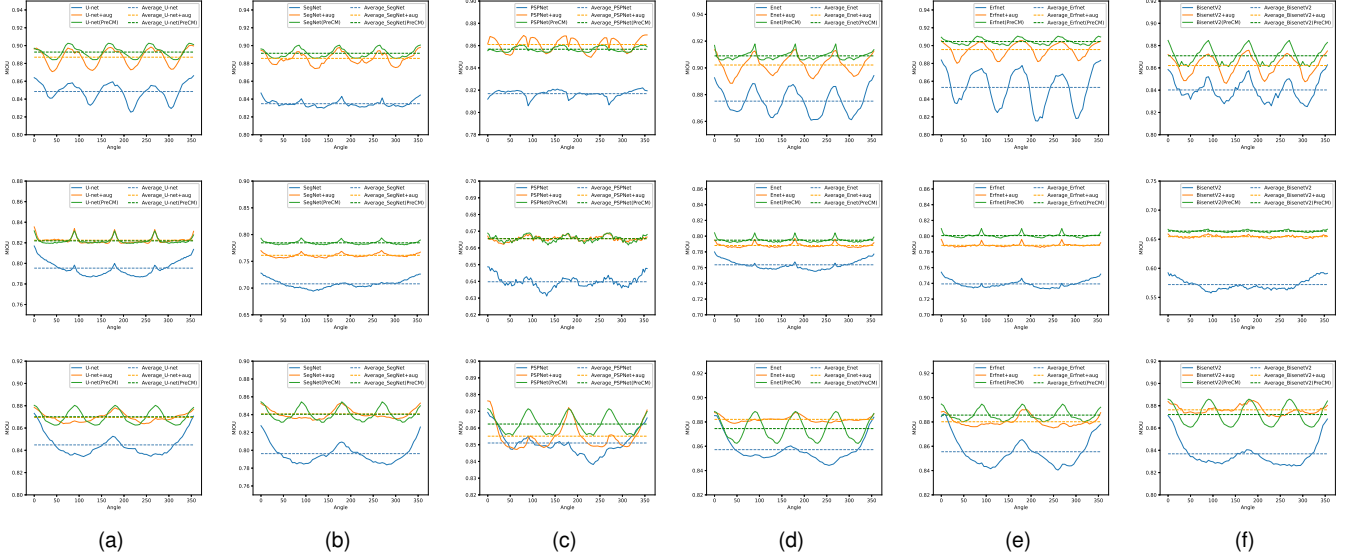


Fig. 14. The MIOU curves of the original, PreCM-based, and data augmentation-based networks under different rotation angles (i.e., $[0^\circ, 360^\circ]$). (a) The networks related to U-net; (b) The networks related to SegNet; (c) The networks related to PSPNet; (d) The networks related to Enet; (e) The networks related to BisenetV2. The first, second, and third rows are respectively the results of Satellite Images of Water Bodies, DRIVE, and Floodnet.

to the original networks, the PreCM-based networks still have better segmentation performance on this dataset. In detail, when the test images are not rotated (i.e., 0°), the values obtained by them are greater than that obtained by the original networks. Once more, this implies, in terms of common non-rotating image segmentation task, PreCM is superior over traditional convolutions. However, as long as the test images are rotated, for original networks, the segmentation results decrease dramatically. For example, the IOU value decrease from 0.7769 to 0.7141 for U-net, when the test images are rotated 90° . In contrast, for the PreCM-based U-net, their results are unchanged no matter whether the test images are rotated 90° . Besides, the RD values of all original networks are much higher than that of PreCM-based networks due to the complexity of multi-class samples. So, the effectiveness of PreCM is verified again.

Similarly, we hereinafter compare the PreCM replacement with the data augmentation technology. Seeing Table II, it can be seen that the data augmentation-based networks and the PreCM-based networks are neck and neck. However, in terms of RD values, the differences are quite obvious between them. Clearly, it proves the effectiveness of PreCM. Besides, in Table II, we also calculate the average values of the metrics under these three datasets. Once more, the average values of IOU, MIOU, DICE, and RD prove that PreCM can get comparable or even better performance than data augmentation.

Figs. 12 and 13 accordingly show some visual results of this dataset. For original networks, the segmentation results are satisfactory when the images are not rotated, yet become worse once the images are rotated. Similarly, the performance of data augmentation-based networks when the images are rotated is not satisfactory as well. From the difference maps, we can further demonstrate this point. But, for the PreCM-based networks, the segmentation results are really better and

unchanged due to the rotation equivariance of PreCM.

D. Discussion of the Other Rotation Angles

In the former subsection, we have demonstrated the rotation equivariance of PreCM at $\{0^\circ, 90^\circ, 180^\circ, 270^\circ\}$. Without losing generality, next, we discuss the performance of PreCM in other rotation angles. To this end, Fig. 14 draws the MIOU curves of these networks from 0° to 360° , where the first, second, and third rows respectively denote the results of Satellite Images of Water Bodies, DRIVE, and Floodnet.

From Fig. 14, it can be seen that for all networks, their PreCM versions obviously hold better MIOU curves than original versions. So, this directly verifies that, in terms of other rotation angles, our PreCM is still effective. Through comparing the PreCM-based networks and the data augmentation-based networks, one can find that, for common and small sample binary segmentation tasks, the MIOU values of former are greater than that of latter in most cases, which can be further demonstrated by the dashed lines (i.e., average MIOU). At the same time, the MIOU curves of PreCM-based networks have a much smaller fluctuation than the data augmentation-based approaches. However, for the multi-class segmentation task (i.e., the third row), although the average MIOU values of former are comparable to the latter, the curve fluctuations of PreCM-based networks are a little severe than that of augmentation-based networks. This may be due to the complexity of multi-class segmentation task and sample imbalance issue.

Overall, no matter for $\{0^\circ, 90^\circ, 180^\circ, 270^\circ\}$ or the other rotation angles, the PreCM-related networks show a comparable or even better segmentation accuracy than the data augmentation-based networks. But, in terms of training samples, the number of the training samples of former is just 1/4 of latter.

V. CONCLUSION

In this paper, we proposed a new rotation equivariant convolution mode PreCM, wherein the padding-based convolution group was mainly utilized to achieve rotation equivariance under feature maps and convolutions of different scales as well as networks of different hyperparameters. Since our PreCM was obtained by a series of mathematical deductions, it can be directly used to replace classical convolutions, such as dilated convolution, transposed convolution, variable stride convolution, and flattened convolution, for making the networks rotation equivariant. To test the effectiveness of PreCM, three classical semantic segmentation networks: U-net, Segnet, PSPNet, and three lightweight semantic networks: Enet, Erfnet, BisenetV2 were further chosen as the basic segmentation networks. The experimental results carried out on three datasets showed that the PreCM-based networks not only have rotation equivariance, but also hold better segmentation performance than the original and data augmentation-based networks. Further research should be performed to explore more different kinds of \otimes_{σ_i} .

REFERENCES

- [1] Z. Liu, X. Li, P. Luo, C. C. Loy, and X. Tang, "Deep learning markov random field for semantic segmentation," *IEEE Transactions on Pattern Analysis and Machine Intelligence*, vol. 40, no. 8, pp. 1814–1828, 2017.
- [2] B. Li, S. Liu, W. Xu, and W. Qiu, "Real-time object detection and semantic segmentation for autonomous driving," in *MIPPR 2017: Automatic Target Recognition and Navigation*, vol. 10608. SPIE, 2018, pp. 167–174.
- [3] B. Dang and Y. Li, "Msresnet: Multiscale residual network via self-supervised learning for water-body detection in remote sensing imagery," *Remote Sensing*, vol. 13, no. 16, p. 3122, 2021.
- [4] G. L. Oliveira, W. Burgard, and T. Brox, "Efficient deep models for monocular road segmentation," in *IEEE/RSJ International Conference on Intelligent Robots and Systems (IROS)*, 2016, pp. 4885–4891.
- [5] X. Tao, D. Zhang, W. Ma, X. Liu, and D. Xu, "Automatic metallic surface defect detection and recognition with convolutional neural networks," *Applied Sciences*, vol. 8, no. 9, p. 1575, 2018.
- [6] X. Hai-xiang, Z. Guang-xi, T. Jin-wen, Z. Xiang, and P. Fu-yuan, "Image segmentation based on support vector machine," *Journal of Electronic Science and Technology*, vol. 3, no. 3, pp. 226–230, 2005.
- [7] B. Kang and T. Q. Nguyen, "Random forest with learned representations for semantic segmentation," *IEEE Transactions on Image Processing*, vol. 28, no. 7, pp. 3542–3555, 2019.
- [8] Z. Kato and T.-C. Pong, "A markov random field image segmentation model for color textured images," *Image and Vision Computing*, vol. 24, no. 10, pp. 1103–1114, 2006.
- [9] N. Plath, M. Toussaint, and S. Nakajima, "Multi-class image segmentation using conditional random fields and global classification," in *International Conference on Machine Learning*, 2009, pp. 817–824.
- [10] X. Wei, S. Su, Y. Wei, and X. Lu, "Rotational convolution: Rethinking convolution for downside fisheye images," *IEEE Transactions on Image Processing*, 2023.
- [11] J. Long, E. Shelhamer, and T. Darrell, "Fully convolutional networks for semantic segmentation," in *Proceedings of the IEEE Conference on Computer Vision and Pattern Recognition*, 2015, pp. 3431–3440.
- [12] L.-C. Chen, G. Papandreou, I. Kokkinos, K. Murphy, and A. L. Yuille, "Deepplab: Semantic image segmentation with deep convolutional nets, atrous convolution, and fully connected crfs," *IEEE Transactions on Pattern Analysis and Machine Intelligence*, vol. 40, no. 4, pp. 834–848, 2017.
- [13] M. Yang, K. Yu, C. Zhang, Z. Li, and K. Yang, "Denseaspp for semantic segmentation in street scenes," in *Proceedings of the IEEE Conference on Computer Vision and Pattern Recognition*, 2018, pp. 3684–3692.
- [14] D. K. Gupta, D. Arya, and E. Gavves, "Rotation equivariant siamese networks for tracking," in *Proceedings of the IEEE Conference on Computer Vision and Pattern Recognition*, 2021, pp. 12 362–12 371.
- [15] A. Mikołajczyk and M. Grochowski, "Data augmentation for improving deep learning in image classification problem," in *International Interdisciplinary PhD Workshop (IIPhDW)*. IEEE, 2018, pp. 117–122.
- [16] J. Choi, T. Kim, and C. Kim, "Self-ensembling with gan-based data augmentation for domain adaptation in semantic segmentation," in *Proceedings of the IEEE International Conference on Computer Vision*, 2019, pp. 6830–6840.
- [17] V. Olsson, W. Tranheden, J. Pinto, and L. Svensson, "Classmix: Segmentation-based data augmentation for semi-supervised learning," in *Proceedings of the IEEE Winter Conference on Applications of Computer Vision*, 2021, pp. 1369–1378.
- [18] D. Laptev, N. Savinov, J. M. Buhmann, and M. Pollefeys, "Ti-pooling: transformation-invariant pooling for feature learning in convolutional neural networks," in *Proceedings of the IEEE Conference on Computer Vision and Pattern Recognition*, 2016, pp. 289–297.
- [19] T. Cohen and M. Welling, "Group equivariant convolutional networks," in *International Conference on Machine Learning*. ICML, 2016, pp. 2990–2999.
- [20] J. Li, Z. Yang, H. Liu, and D. Cai, "Deep rotation equivariant network," *Neurocomputing*, vol. 290, pp. 26–33, 2018.
- [21] D. Romero, E. Bekkers, J. Tomczak, and M. Hoogendoorn, "Attentive group equivariant convolutional networks," in *International Conference on Machine Learning*. PMLR, 2020, pp. 8188–8199.
- [22] L. He, Y. Chen, Y. Dong, Y. Wang, Z. Lin *et al.*, "Efficient equivariant network," *Advances in Neural Information Processing Systems*, vol. 34, pp. 5290–5302, 2021.
- [23] D. Marcos, M. Volpi, N. Komodakis, and D. Tuia, "Rotation equivariant vector field networks," in *Proceedings of the IEEE International Conference on Computer Vision*, 2017, pp. 5048–5057.
- [24] W. Sun and R. Wang, "Fully convolutional networks for semantic segmentation of very high resolution remotely sensed images combined with dsm," *IEEE Geoscience and Remote Sensing Letters*, vol. 15, no. 3, pp. 474–478, 2018.
- [25] O. Ronneberger, P. Fischer, and T. Brox, "U-net: Convolutional networks for biomedical image segmentation," in *Medical Image Computing and Computer-Assisted Intervention—MICCAI*. Springer, 2015, pp. 234–241.
- [26] V. Badrinarayanan, A. Kendall, and R. Cipolla, "Segnet: A deep convolutional encoder-decoder architecture for image segmentation," *IEEE Transactions on Pattern Analysis and Machine Intelligence*, vol. 39, no. 12, pp. 2481–2495, 2017.
- [27] H. Zhao, J. Shi, X. Qi, X. Wang, and J. Jia, "Pyramid scene parsing network," in *Proceedings of the IEEE Conference on Computer Vision and Pattern Recognition*, 2017, pp. 2881–2890.
- [28] L.-C. Chen, G. Papandreou, I. Kokkinos, K. Murphy, and A. L. Yuille, "Deepplab: Semantic image segmentation with deep convolutional nets, atrous convolution, and fully connected crfs," *IEEE Transactions on Pattern Analysis and Machine Intelligence*, vol. 40, no. 4, pp. 834–848, 2017.
- [29] A. Paszke, A. Chaurasia, S. Kim, and E. Culurciello, "Enet: A deep neural network architecture for real-time semantic segmentation," *Proceedings of the IEEE Conference on Computer Vision and Pattern Recognition*, 2016.
- [30] E. Romera, J. M. Alvarez, L. M. Bergasa, and R. Arroyo, "Erfnnet: Efficient residual factorized convnet for real-time semantic segmentation," *IEEE Transactions on Intelligent Transportation Systems*, vol. 19, no. 1, pp. 263–272, 2017.
- [31] C. Yu, C. Gao, J. Wang, G. Yu, C. Shen, and N. Sang, "Bisenet v2: Bilateral network with guided aggregation for real-time semantic segmentation," *International Journal of Computer Vision*, vol. 129, pp. 3051–3068, 2021.
- [32] Y. Wang, Q. Zhou, J. Liu, J. Xiong, G. Gao, X. Wu, and L. J. Latecki, "Lednet: A lightweight encoder-decoder network for real-time semantic segmentation," in *IEEE International Conference on Image Processing (ICIP)*. IEEE, 2019, pp. 1860–1864.
- [33] D. Marcos, M. Volpi, N. Komodakis, and D. Tuia, "Rotation equivariant vector field networks," in *Proceedings of the IEEE International Conference on Computer Vision*, 2017, pp. 5048–5057.
- [34] C. Deng, O. Litany, Y. Duan, A. Poulenard, A. Tagliasacchi, and L. J. Guibas, "Vector neurons: A general framework for so(3)-equivariant networks," in *Proceedings of the IEEE International Conference on Computer Vision*, 2021, pp. 12 200–12 209.
- [35] J. Han, J. Ding, N. Xue, and G.-S. Xia, "Redet: A rotation-equivariant detector for aerial object detection," in *Proceedings of the IEEE Conference on Computer Vision and Pattern Recognition*, 2021, pp. 2786–2795.
- [36] M. Weiler, F. A. Hamprecht, and M. Storath, "Learning steerable filters for rotation equivariant cnns," in *Proceedings of the IEEE Conference on Computer Vision and Pattern Recognition*, 2018, pp. 849–858.
- [37] Y. Ma, Y. Luo, and Z. Yang, "Pcfnet: Deep neural network with predefined convolutional filters," *Neurocomputing*, vol. 382, pp. 32–39, 2020.
- [38] V. Dumoulin and F. Visin, "A guide to convolution arithmetic for deep learning," *International Conference on Machine Learning*, 2016.
- [39] F. Escobar, "Satellite images of water bodies," <https://www.cvmar.net/dataSets/detail/736>.
- [40] J. Staal, M. D. Abràmoff, M. Niemeijer, M. A. Viergever, and B. Van Ginneken, "Ridge-based vessel segmentation in color images of the retina," *IEEE Transactions on Medical Imaging*, vol. 23, no. 4, pp. 501–509, 2004.
- [41] M. Rahnemoonfar, T. Chowdhury, A. Sarkar, D. Varshney, M. Yari, and R. R. Murphy, "Floodnet: A high resolution aerial imagery dataset for post flood scene understanding," *IEEE Access*, vol. 9, pp. 89 644–89 654, 2021.
- [42] S. K. McFeeters, "The use of the normalized difference water index (ndwi) in the delineation of open water features," *Remote Sensing*, vol. 17, no. 7, pp. 1425–1432, 1996.
- [43] P. Shi, M. Duan, L. Yang, W. Feng, L. Ding, and L. Jiang, "An improved u-net image segmentation method and its application for metallic grain size statistics," *Materials*, vol. 15, no. 13, p. 4417, 2022.